Proceedings of the ASME 2025
Aerospace Structures, Structural Dynamics, and Materials Conference
SSDM2025
May 5–7, 2025, Houston, TX

SSDM2025-152052

A COMPREHENSIVE NUMERICAL MODELLING OF A BENCHMARK WIND TURBINE BLADE

Francisco Vieira [1], Mertol Tüfekci [2 3] *, Sam Patel [1], Soraia Pimenta [1]

[1] Department of Mechanical Engineering, Imperial College London, South Kensington Campus, London, SW7 2AZ, UK
[2] Centre for Engineering Research, University of Hertfordshire, Hatfield AL10 9AB, UK
[3] School of Physics, Engineering and Computer Science, University of Hertfordshire, Hatfield, Hertfordshire AL10 9AB, UK

ABSTRACT

Wind energy plays a crucial role in mitigating the environmental impact of modern society. As reliance on wind energy grows, ensuring the structural integrity of wind turbine blades becomes increasingly important. This is the main driving motivation for the development of advanced monitoring and modelling techniques capable of providing accurate and efficient predictions of blade behaviour. This study focuses on the application of finite element modelling to characterise wind turbine blades, with particular emphasis on the DTU 10MW Reference Wind Turbine—a shell model of an 89.2 m blade. The structural response of the blade is examined under various loading conditions, with increasing model complexity achieved through the incorporation of non-linear effects and damage mechanisms. Using Hashin's damage criterion and the energy dissipation-based damage evolution law, a progressive failure analysis reveals valuable insights into localised damage regions and stress concentrations. These findings highlight the need for further refinement to enhance model accuracy and reliability.

Keywords: Wind turbine blades, mechanics of composites, finite element-based tools, progressive failure analysis

NOMENCLATURE

Roman Letters
BECAS BEam Cross-section Analysis Software
BEMT Blade Element Momentum Theory
CAE Computer-Aided Engineering
CDM Continuum Damage Mechanics
CFD Computational Fluid Dynamics
DE Damage Evolution
DTU Technical University of Denmark
GFRP Glass Fibre Reinforced Polymer
Nlgeom Non-linear geometric analysis
PFA Progressive Failure Analysis
RWT Reference Wind Turbine
WTB Wind Turbine Blade

Greek Letters
ρ Material density
ν Poisson's ratio
σ Stress
ε Strain
γ Shear strain
α Coefficient for shear stress influence on tensile failure

Subscripts
1 Fibre direction
2 Transverse direction
3 Through-thickness direction
T Tensile property
C Compressive property
L Longitudinal direction
S Shear property

Dimensionless Numbers and Other Symbols
F_f^t Damage initiation criterion for fibre tension
F_f^c Damage initiation criterion for fibre compression
F_m^t Damage initiation criterion for matrix tension
F_m^c Damage initiation criterion for matrix compression
d_f Damage variable for fibre failure
d_m Damage variable for matrix failure
d_s Damage variable for shear failure
D Denominator term in stiffness degradation matrix
$\mathbf{C}_d$ Damaged stiffness matrix

Units
kg/m^3 Kilogram per cubic metre (density)
GPa Gigapascal (elastic modulus, shear modulus)
MPa Megapascal (stress, strength)
J/m^2 Joules per square metre (fracture energy)

*Corresponding author: m.tufekci@herts.ac.uk

1. INTRODUCTION

The global energy sector is transitioning towards renewable sources to meet the rising demand for clean energy. Wind energy, noted for its low operating costs and abundant availability, is a leading renewable energy source [1]. Many countries have initiated policies to accelerate wind energy adoption; for instance, the European Union aims to boost offshore wind production from 12 GW in 2020 to 60 GW by 2030 and 300 GW by 2050 [2], stressing the crucial role of wind technologies for a sustainable future.

Wind turbine blades (WTBs) are essential for the reliability and efficiency of wind energy. WTBs are large composite structures designed to endure extreme conditions for 20 to 25 years, yet there is no precise model for determining when decommissioning is required [3].

Modelling approaches for WTBs include analytical beam-based methods and computational finite element simulations. These models predict blade behaviour using data from manufacturing and in-service monitoring, guiding decisions in design, operational life, and decommissioning [4]. However, creating a computationally efficient yet accurate model remains challenging due to the complex geometry and material anisotropy of WTBs.

Analytical models, typically based on simplifying assumptions about materials, range from elastic behaviour to complex damage propagation. Taglialegne used Euler-Bernoulli beam theory to study stress in thin-walled blades, gradually introducing more realistic geometry [5]. Another approach involves cross-sectional homogenisation for variable beam sections to derive effective elastic properties [6].

Failure initiation is challenging to model accurately due to limited experimental data [7]. Recent studies using actuators and vibration sensors have sought to detect damage in full-scale WTBs [8]. Common failure criteria, including maximum strain, stress, and Tsai–Wu theories, are used to assess blade integrity through post-processing stress data [9].

Damage propagation modelling is more complex, often involving both static and dynamic loading scenarios. Studies have applied Continuum Damage Mechanics (CDM) for characterising damage in WTBs [10, 11]. For instance, Bhangale [10] applied CDM using thermodynamic processes, while others coupled CDM with computational micromechanics to simulate fatigue [11]. Despite CDM's accuracy, simpler stress-life (S-N) methods are still used for fatigue analysis, although they have inherent limitations regarding real-world accuracy [11–13].

Multi-continuum theory combined with kinetic fracture theory provides another perspective on damage propagation. Greaves demonstrated that separating matrix and fibre stresses helps predict initial failure in the matrix, offering insight into failure progression [14].

The finite element method is a standard tool for understanding WTB stress distribution. 3D solid elements are used for detailed analysis but are computationally expensive, making them impractical for design processes [15, 16]. Alternatively, shell elements are a popular choice for capturing overall structural behaviour efficiently [17]. Shell elements are also effective for incorporating bending-twist coupling, which is crucial for understanding torsional behaviour in blades [15, 18]. Beam elements offer another option, although they cannot capture local buckling effects. Nonetheless, geometrically exact beam models can accurately predict global blade response when properly parameterised with cross-sectional properties derived using tools like BECAS [19, 20].

BECAS, a 2D FE-based analysis tool, is highly effective for calculating the mass and stiffness properties of WTBs. It can capture material anisotropy and is integrated with Abaqus for efficient beam model generation, making it suitable for larger-scale analysis [19, 21].

Typically, WTB models apply loads at the blade tip or along its length, though this can create stress concentrations. More sophisticated modelling approaches employ Computational Fluid Dynamics (CFD) or Blade Element Momentum Theory (BEMT) to generate realistic aerodynamic load distributions. However, CFD is computationally slow, and BEMT lacks detailed stress predictions within composite layers. A recent study proposed an efficient method for integrating aerodynamic loads into 3D models, accounting for blade deformation effects [22].

Advanced fracture mechanics are increasingly used to simulate crack initiation, propagation, and inter-laminar failures [23]. These methods are essential for evaluating WTB durability under operational loads, given their susceptibility to multiple simultaneous failure modes [4, 24].

The objective of this research is to develop progressively complex models of WTBs, starting from simplified models that converge rapidly to more advanced models that offer higher fidelity in predicting structural behaviours, though with increased computational demands. The initial models assume elastic material behaviour and focus on capturing the basic structural response under idealised conditions. As complexity is introduced, non-linear effects such as progressive damage, fatigue behaviour, and interactions between multiple failure modes are integrated. Advanced modelling techniques are employed, including CDM and cross-sectional analysis tools like BECAS, which facilitate accurate representation of material anisotropy and inhomogeneity. The ultimate goal is to achieve a balance between computational efficiency and model accuracy, especially using methods like shell elements and advanced fracture mechanics that cater to different scales of analysis. By progressively refining the structural analysis and material modelling techniques of WTBs, this study aims to guide the wind industry toward solutions that are not only structurally optimised for increased efficiency and durability but are also environmentally conscious in terms of end-of-life management. The detailed exploration of various finite element approaches, from 3D solid and shell elements, ensures that each technique's applicability and limitations are clearly established. Moreover, the application of advanced methods like Hashin's damage criterion for failure initiation and energy dissipation-based evolution laws for damage propagation provide critical insights into failure mechanisms, stress concentrations, and localised damage under different loading scenarios. These findings are essential for designing blades that meet operational demands and can withstand the extreme conditions they face over their long service lives, ultimately contributing to the reliable growth of wind energy technology.

2. DESCRIPTION OF DTU 10MW REFERENCE WIND TURBINE BLADE

The next step is to start working with an actual WTB model. The base model used in this study is the DTU 10MW-RWT. DTU Wind Energy was responsible for the development of several wind turbine analysis software tools that are used to design the DTU 10MW-RWT, and that are used commercially.

2.1 Finite Element Model of DTU 10MW Reference Wind Turbine Blade

The blade is constructed as a reference to compare high fidelity simulations, airfoil designs and wind turbine optimisation strategies. The geometry and mesh structure is shown in Figure 1 (explained in more detail in Bak et al. [25]), and its shell model and layup definitions are derived from the official DTU database.

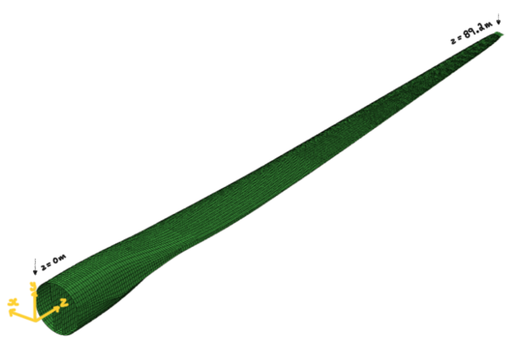

FIGURE 1: DTU 10MW-RWT BLADE MODEL IN ABAQUS

2.2 Material Properties

The DTU 10MW-RWT is composed of Glass Fibre Reinforced Polymer (GFRP) plies (uniaxial, biaxial and triaxial) and balsa as sandwich core material. The material properties of the GFRP plies and balsa are listed in Table 1, where ρ is the material density, E indicates the modulus of elasticity, G denotes the shear modulus, ν stands for the Poisson's ratio, and subscripts 1, 2, and 3 indicate directions along the coordinate axes used. X_T and X_C represent the tensile and compressive strengths in the fibre direction, respectively, while Y_T and Y_C denote the tensile and compressive strengths perpendicular to the fibres. S_L and S_T correspond to the longitudinal and transverse shear strengths. A uniaxial ply in the layup is defined with [0°/90°] ply properties with 95% and 5% contribution respectively, a biaxial ply with [+45°/−45°] ply properties with 50% contribution each, and a triaxial ply with [+45°/−45°/0°] ply properties with 35%, 35%, and 30% contribution respectively [26].

The blade is 89.2 m long (axially) and has a 5.4 m root diameter. The main load carrying structure consists of a box grinder design, based on two caps and two shear webs (Caps, Web A and Web B), surrounded by adhesively connected panels that form the aerodynamic surface (Leading Panels, Nose, Trailing Panels, Web C, Tail A, Tail B, Tail C and Tail V).

TABLE 1: MATERIAL PROPERTIES IMPLEMENTED [26]

S. No	Properties	Uniaxial	Biaxial	Triaxial	Balsa
1	ρ (kg/m^3)	1915.5	1845.0	1683.0	110
2	E_1 (GPa)	41.63	13.92	21.79	0.050
3	E_2 (GPa)	14.93	13.92	14.67	0.050
4	E_3 (GPa)	13.42	12.09	12.09	2.730
5	G_12 (GPa)	5.047	11.50	9.413	0.0167
6	G_23 = G_13 (GPa)	5.0469	4.53	4.53	0.150
7	ν_{12}	0.241	0.533	0.478	0.5
8	ν_{23}	0.33	0.3329	0.3329	0.013
9	ν_{13}	0.2675	0.275	0.275	0.013
10	X_T (MPa)	903.6	214.2	472.06	-
11	X_C (MPa)	660.1	184.8	324.16	5.4
12	$Y_T = Y_C$ (MPa)	42.1	184.8	127.12	-
13	$S_L = S_T$ (MPa)	58.65	143.9	99.25	-
14	G_{FT} (J/m^2)	1200	1200	1200	-
15	$G_{FC} = G_{MT} = G_{MC}$ (J/m^2)	4000	4000	4000	-

2.3 Layup Definitions

In terms of layup definitions, the blade is divided into 100 regions axially and 11 regions circumferentially, which correspond to the 11 different composite layups that make up the blade. It also shows the box grinder structure connected to the airfoil panels. In addition, the circumferential arrangement of the layups varies between cross-sections along the axial position of the blade. The positioning of the layups are shown in Figure 2.

Each layup presented is made of a combination of the four materials described previously in Table 1. The differences in the thicknesses and arrangements of these materials along the sections of the blade significantly influence its structural properties. The graph below (Figure 3) illustrates the distribution of the material thicknesses of the blade along its axial position (from Section 1 to Section 100).

In addition, every layup is composed of specific combinations and orientations of uniaxial, biaxial and triaxial plies, and balsa, and so exhibits unique mechanical properties. Therefore, it is highly important to characterise each layup separately in order to gain a comprehensive understanding of their individual contributions to the blade's overall performance.

For further research purposes, below are listed the names of the 11 layups and their given names according to the DTU imported CAE file (Table 2).

3. DAMAGE ANALYSIS

3.1 Damage Criteria

In this study, damage to the blade is analysed using Hashin's damage criterion along with the energy dissipation-based damage evolution law. This framework addresses intra-ply damage mechanisms in composite materials. Other damage mechanisms, such as debonding and delamination, are not included in the model.

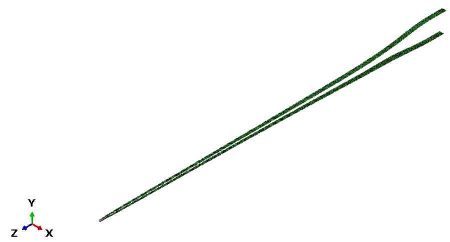

(a) Caps

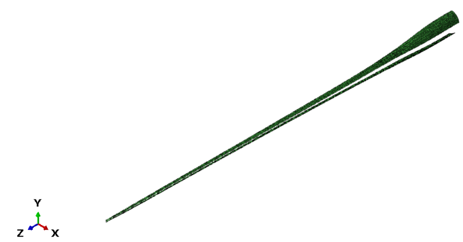

(b) Leading Panels

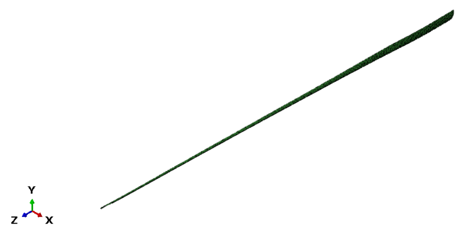

(c) Nose

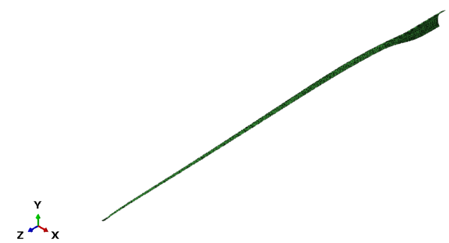

(d) Tail A, Tail B, Tail C and Tail V

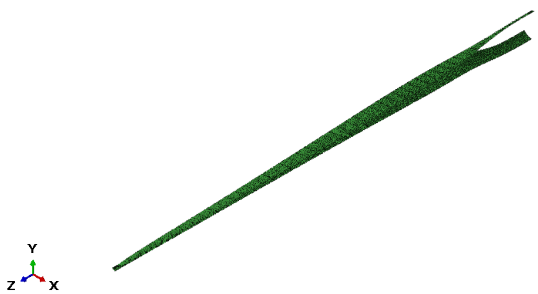

(e) Trailing Panels

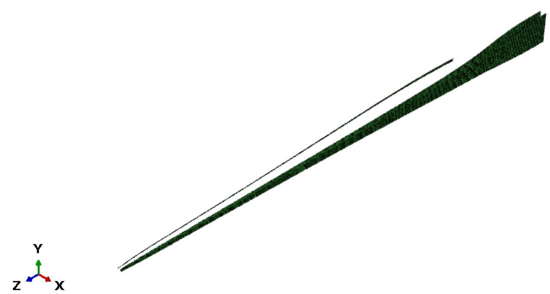

(f) Web A, Web B and Web C

FIGURE 2: COMPOSITE LAYUPS IN ABAQUS

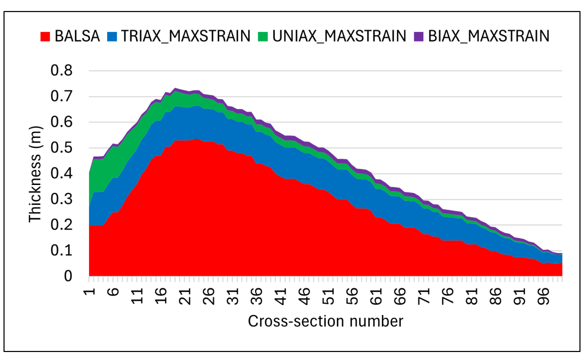

FIGURE 3: SUM OF LAYUP THICKNESSES ALONG THE AXIAL POSITION OF THE DTU 10MW-RWT

TABLE 2: COMPOSITE LAYUPS

Layup	Layup name in blade model
Caps	CA
Leading panels	LP
Nose	NO
Tail A	TA
Tail B	TB
Tail C	TC
Trailing Panels	TP
Tail V	TV
Web A	WA
Web B	WB
Web C	WC

3.2 Damage Initiation Framework

In Abaqus, the criteria for damage initiation for fibre reinforced composites is based on Hashin's theory [27, 28]. It considers four different mechanisms for damage initiation (shown below), which have the following general forms [29]:

Fibre tension ($\hat{\sigma}_{11} \geq 0$):

$$F_f^t = \left(\frac{\hat{\sigma}_{11}}{X_T}\right)^2 + \alpha \left(\frac{\hat{\tau}_{12}}{S_L}\right)^2 \tag{1}$$

Fibre compression ($\hat{\sigma}_{11} < 0$):

$$F_f^c = \left(\frac{\hat{\sigma}_{11}}{X_C}\right)^2 \tag{2}$$

Matrix tension ($\hat{\sigma}_{22} \geq 0$):

$$F_m^t = \left(\frac{\hat{\sigma}_{22}}{Y_T}\right)^2 + \left(\frac{\hat{\tau}_{12}}{S_L}\right)^2 \tag{3}$$

Matrix compression ($\hat{\sigma}_{22} < 0$):

$$F_m^c = \left(\frac{\hat{\sigma}_{22}}{2S_T}\right)^2 + \left[\left(\frac{Y_C}{2S_T}\right)^2 - 1\right]\frac{\hat{\sigma}_{22}}{Y_C} + \left(\frac{\hat{\tau}_{12}}{S_L}\right)^2 \tag{4}$$

In the above equations, the coefficient α accounts for the influence of shear stress on the fibre tensile initiation criteria (for this analysis, $\alpha = 0$). The outputs in Abaqus that correspond to these variables are HSNFCCRT, HSNFTCRT, HSNMCCRT and HSNMTCRT respectively. These only provide insights into how close the material is to the point of damage initiation, which happens when one of the output variables exceeds 1 ($F_i \geq 1$, where subscript i stands for one of the four damage mechanisms).

3.3 Damage Evolution Framework

The criteria for damage evolution is energy-based [30, 31] and takes into account the material's stiffness degradation by recomputing the damaged stiffness matrix ($\mathbf{C}_d$) as such [29]:

$$\mathbf{C}_d = \frac{1}{D}\begin{bmatrix} \frac{1-d_f}{E_1} & \frac{(1-d_f)(1-d_m)\nu_{12}}{E_1} & 0 \\ \frac{(1-d_f)(1-d_m)\nu_{21}}{E_2} & \frac{1-d_m}{E_2} & 0 \\ 0 & 0 & \frac{1-d_s}{G} \end{bmatrix} \tag{5}$$

The relationship between stress (σ) and strain (ε) is expressed as $\sigma = \mathbf{C}_d\varepsilon$. Note that $D = 1 - (1-d_f)(1-d_m)\nu_{12}\nu_{21}$, and d_f, d_m, and d_s represent the present state of fibre, matrix and shear damage, respectively. Also, E_1, E_2, G, ν_{12} and ν_{21} are elasticity constants and the damage variables d_f, d_m, and d_s are calculated from the variables d_f^t, d_f^c, d_m^t, and d_m^c, which correspond to the four failure modes:

$$d_f = \begin{cases} d_f^t & \text{if } \hat{\sigma}_{11} \geq 0, \\ d_f^c & \text{if } \hat{\sigma}_{11} < 0 \end{cases} \tag{6}$$

$$d_m = \begin{cases} d_m^t & \text{if } \hat{\sigma}_{22} \geq 0, \\ d_m^c & \text{if } \hat{\sigma}_{22} < 0 \end{cases} \tag{7}$$

$$d_s = 1 - (1-d_f^t)(1-d_f^c)(1-d_m^t)(1-d_m^c) \tag{8}$$

$\hat{\sigma}_{11}$ and $\hat{\sigma}_{22}$ are components of the effective stress tensor. In this case, the output variables for damage evolution in Abaqus are DAMAGEFC, DAMAGEFT, DAMAGEMC and DAMAGEMT, respectively. These parameters provide information on the evolution of damage in the material. Their value can range from $0 \leq d_i \leq 1$, where once again subscript i stands for one of the four damage mechanisms, and can be interpreted as follows:

- $d_i = 0$ - No damage. Undamaged state.
- $0 < d_i < 1$ - Progressive damage. Material has initiated damage and is undergoing stiffness reduction. The value represents the extent of the damage (and associated stiffness reduction).
- $d_i = 1$ - Complete damage. Material has reached ultimate failure in its respective damage mode. The material can no longer carry load in the damaged mode because its stiffness in that mode is completely degraded.

4. VALIDATION WITH LITERATURE

The DTU 10MW-RWT CAE model is validated with existing literature to ensure it is correctly implemented.

4.1 Simple Loading Cases

Initially, the blade is subjected to two simple loading cases, "Gravity" and "Concentrated force at the tip of $F = -5000\,N$ in flapwise direction".

To impose the boundary condition of the concentrated force at the tip two methodologies are explored. Method 1 consisted in dividing the total force by the number of nodes at the tip cross-section and applying that resulting force ($F_{new} = \frac{-5000}{54} = -92.6\,N$) at each node. Method 2 involved imposing a kinematic coupling on the nodes at the tip's cross-section to the section's half-chord point and applying the total concentrated force at that point.

4.2 Loading Cases from Blasques et al. [19]

Then, for a reliable validation of the results, the work of Blasques et al. [19] is used as comparison, which adopts exactly the same blade model (the DTU 10MW-RWT) for research. That study analysed two loading cases (BLC1 and BLC2), shown schematically in Figure 4.

The concentrated forces (f_x and f_y) and the moments (m_z) are applied at the axial position (z) specified in Table 3 at the half-chord point of the corresponding cross-section (similarly to the application of the concentrated force in Method 2 of Section 4.1).

The displacements of the blade are read from particular points that lie on certain paths that consist of a group of nodes on the mesh of the blade. Each path is defined individually and assigned a set in the *Assembly* module. To achieve this, each point is matched to its corresponding node in the mesh at the root of the blade, and then their adjacent nodes in the longitudinal direction are selected to progressively create a path. The paper used to validate the results (Blasques et al. [19]) does not specify how these paths are defined, thus these path definitions are an approximation and could be a potential source of error. The path definitions in Abaqus are shown in Figure 5. These sets are then accessed in the *Visualisation* module and used to plot the relevant results.

TABLE 3: VALUES OF THE LOADS AND MOMENTS APPLIED IN THE LOADING CASES IN BLASQUES ET AL. [19]

Loading Case	z [m]	20.1	30.4	33.0	47.7	52.0	62.4	65.8	76.2	84.8
BLC1	f_x [kN]	0.0	0.0	290.0	180.0	0.0	130.0	0.0	18.0	25.0
	f_y [kN]	230.0	270.0	0.0	0.0	250.0	0.0	220.0	190.0	165.0
	m_z [kNm]	-122.7	-226.5	-27.1	-8.0	-170.8	-0.6	-111.9	-74.0	-46.9
BLC2	z [m]	89.166								
	m_z [kNm]	450								

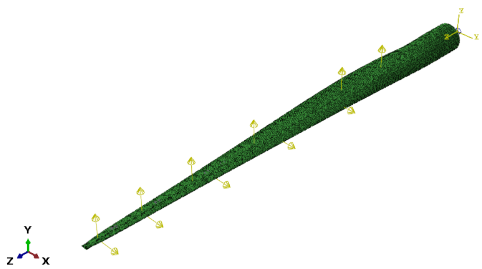

(a) ***BLC1***

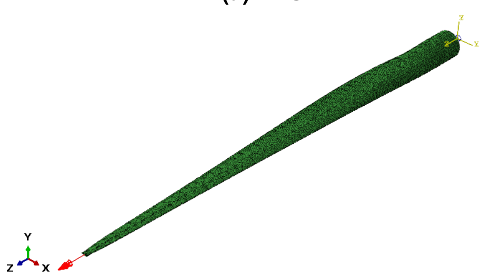

(b) ***BLC2***

FIGURE 4: LOADING CASES APPLIED TO THE DTU 10MW-RWT IN BLASQUES ET AL. [19]

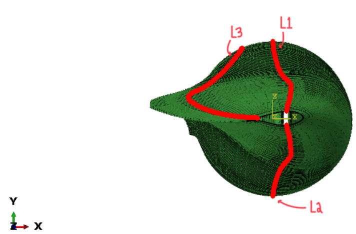

FIGURE 5: LONGITUDINAL PATHS' DEFINITION IN ABAQUS

5. INTRODUCING NON-LINEAR EFFECTS AND DAMAGE: PROGRESSIVE FAILURE ANALYSIS (PFA)

To increase the accuracy and complexity of the model in question, non-linear effects and damage evolution are introduced. Similarly to Section 4, loading conditions *BLC1* and *BLC2* are simulated using three different levels of model complexity for each: linear elastic analysis, non-linear geometric analysis (*Nlgeom*), and non-linear geometric analysis with damage evolution (*Nlgeom w/ DE*). Material properties used in these analyses are defined in Table 1.

For each loading case, a PFA is conducted to understand the complex failure mechanisms happening in the DTU 10 MW-RWT model. The PFA can be divided into different phases of the composite's structural behaviour throughout its loading history. The initial stage involves modelling the material as linear elastic, assuming undamaged constitutive behaviour. This is followed by identifying the point of damage initiation and analysing the material degrading as damage evolves until it reaches ultimate failure.

6. RESULTS AND DISCUSSION

6.1 Validation with Literature

6.1.1 Simple Loading Cases. Each boundary condition is simulated and the results are shown in Figure 6. According to the literature [19], several concentrated forces applied in a certain ways (in edgewise and flapwise directions along blade's longitudinal axis) can represent the state-of-the-art to simulate wind loads in structural analysis of WTBs. Therefore, Figure 6b represents an initial insight to this approximation, which will be further investigated below.

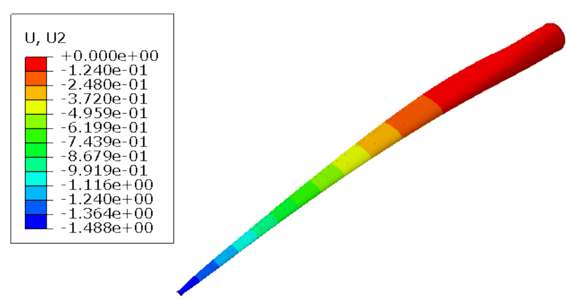

(a) Gravity

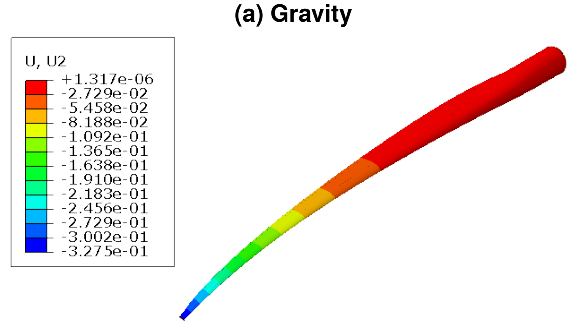

(b) Concentrated force at the tip

FIGURE 6: VERTICAL DISPLACEMENT (M) OF THE DTU 10MW-RWT IN DIFFERENT LOADING CASES

6.1.2 Loading Cases from Blasques et al. [19]. The results obtained from the study are plots of axial strain (ε_{11}) for

BLC1 loading case (Figure 7), and of shear strain (γ_{12}) for *BLC2* loading case (Figure 8), versus the axial position of the blade (z-coordinate). Each graph represents strain extracted from a different path of nodes along the blade's axial position (*L1*, *L2* and *L3*).

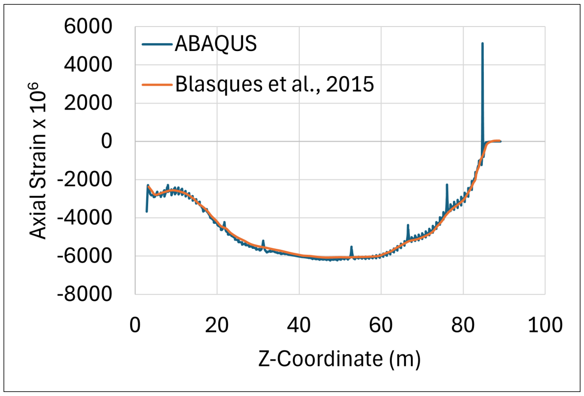

(a) Axial strain (ε_{11}) along path *L1*

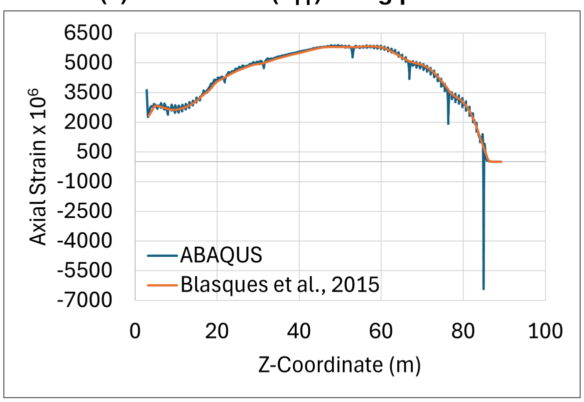

(b) Axial strain (ε_{11}) along path *L2*

FIGURE 7: *BLC1* LOADING CASE DISPLACEMENT CURVES OF THE BLADE

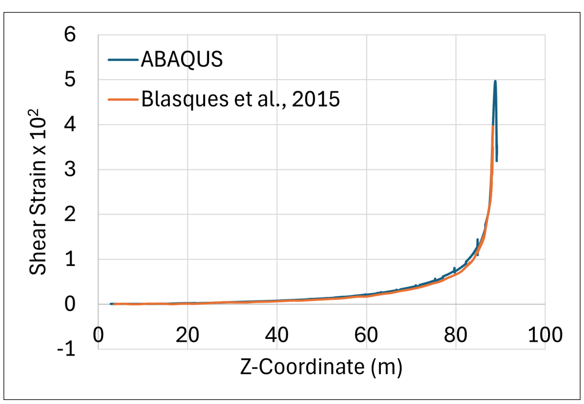

FIGURE 8: SHEAR STRAIN (γ_{12}) ALONG PATH *L3* WITH *BLC2* LOADING CASE

Overall, the results from the author match the ones from the literature. The larger spikes in Figure 7 are strain concentrations that correspond to the position where the concentrated forces (f_y and f_x) are applied. Similarly, the large peak at the end of Figure 8 is due to the boundary condition at the tip where the moment m_z is applied. The smaller oscillations in the plots occur due to the effect of mesh discretisation (where strain varies slightly between adjacent nodes, reflecting local variations in stiffness and/or material properties at nodal points), and geometric discontinuities in the path of nodes selected (such as transitions in cross-sectional area and/or imperfections in the structure of the mesh). Therefore, the plots obtained are correct and any deviation from the literature makes sense in the context of the system analysed. Hence, it is concluded that the validation of the DTU 10MW-RWT model is completed successfully.

6.2 Nonlinear Analysis of the Blade

6.2.1 Load-Displacement Curves. For each loading case, the load-displacement curve of the three analyses is calculated.

Load-Displacement Curve for *BLC1* Loading Case. In the case of *BLC1*, the loading condition consisted of 11 concentrated forces in the edgewise (CF1) and flapwise (CF2) directions and 9 torsional moments (CM3), applied at different axial positions of the blade. The load parameter is calculated by summing algebraically the concentrated forces in each direction, and then adding the values in vectorial form. Similarly, the tip displacement is computed by adding the vectors of displacement (U1, U2 and U3) at Section 100 in the three coordinate directions. As in the previous case, these variables are also predefined in the *Step* module, in the *Field Output* and in the *History Output*. The load-displacement plot is represented in Figure 9.

where i corresponds to a different time instance calculated at every increment of the loading step in Abaqus.

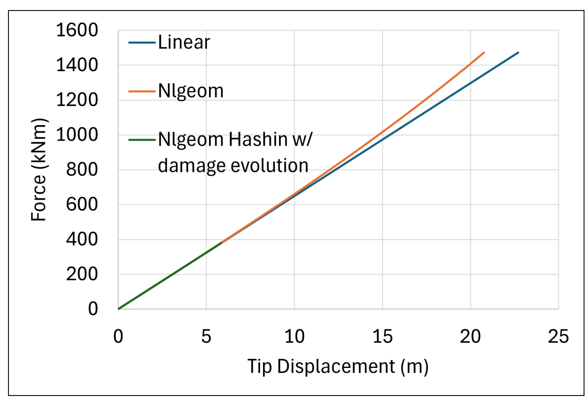

FIGURE 9: LOAD-DISPLACEMENT CURVE FOR *BLC1* LOADING CONDITION

It can be observed that in the load-displacement graph, the *Nlgeom* plot experiences an increase in slope compared to the linear plot at higher values of tip displacement. This indicates that the structure becomes stiffer as the displacement increases, which is characteristic of strain hardening. However, similarly to the previous analysis of the Moment-Tip Rotation, the material properties between the linear and the *Nlgeom* simulations are identical, meaning the material itself is not becoming stiffer. In fact, the non-linear hardening behaviour is also due to the structure being submitted to large deformations, which can have an effect on several key factors related to the geometrical characteristics of the structure, even though the material remains purely elastic. To highlight this effect, the deformed shapes of the DTU 10MW-RWT in the linear and the *Nlgeom* analyses are superposed in Figure 10.

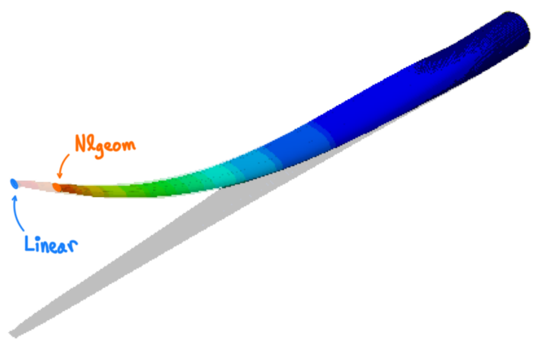

FIGURE 10: DEFORMED SHAPES OF THE DTU 10MW-RWT IN THE LINEAR AND THE *NLGEOM* ANALYSES SUPERPOSED

Large deformations cause significant changes in the geometric configuration of a WTB. This leads to non-linear relationships between the applied loads and the resulting deformations. Specifically, the curvature of beam-like structures becomes non-linear, introducing terms in the equations of motion that are quadratic and cubic in nature. When the blade is deformed, the moment arm (l_m) of the concentrated forces with respect to the root decreases which, in turn, decreases the applied moment. This can be observed in the Moment-Force relationship (Figure 11). Also, Figure 10 clearly shows the reduction in moment arm of the blade schematically. Hence, despite the softening caused by the introduction of geometric non-linearity in the *Nlgeom* analysis, the structural behaviour is dominated by an overall hardening behaviour, mainly because the moment does not increase at the same rate as the force as it is demonstrated by Figure 11.

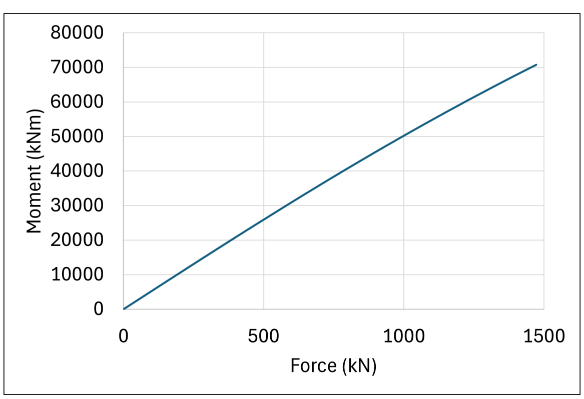

FIGURE 11: MOMENT-FORCE CURVE FOR *NLGEOM* PLOT WITH *BLC1* LOADING CONDITION

In order to obtain closer insight into the blade's structural behaviour, the Load-Displacement curve is plotted independently for edgewise bending (out-of-plane) and flapwise (in-plane) bending. Figure 12 shows that the blade softens in out-of-plane bending and stiffens in in-plane bending, which can be explained by the geometric characteristics of the blade.

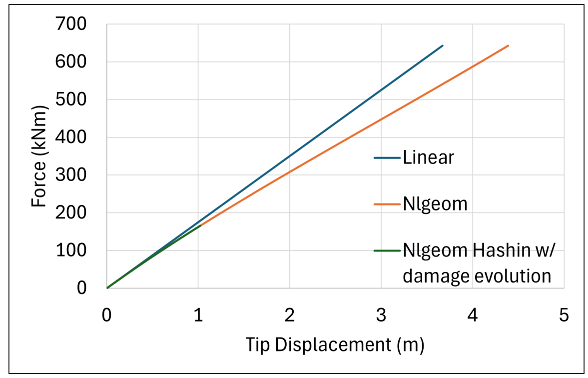

(a) Edgewise bending

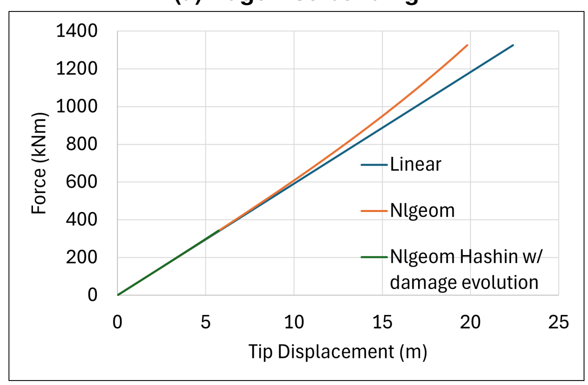

(b) Flapwise bending

FIGURE 12: LOAD-DISPLACEMENT CURVE FOR *BLC1* LOADING CONDITION PLOTTED FOR SEPARATE LOADING DIRECTIONS

The moment of inertia of the blade's cross-sections plays a significant role in how the blade resists bending in different planes. In-plane bending typically involves bending about the axis with a higher moment of inertia while out-of-plane bending usually involves bending about the axis with a lower moment of inertia. This difference in the moment of inertia leads to different bending stiffnesses in the two planes. A higher moment of inertia means higher effective stiffness (hardening), while a lower moment of inertia results in lower effective stiffness (softening).

In-plane (non-pure) bending can cause axial forces in the blade, especially if the blade is fixed or has certain boundary conditions that prevent lateral movement. These axial forces can increase the stiffness of the blade in-plane due to a phenomenon known as geometric stiffening. Essentially, the in-plane deformation induces axial tension forces that can increase the resistance to further bending (hardening).

In out-of-plane bending, the blade might be more prone to shear deformations, which can contribute to a softening effect. Shear deformations are more significant in beams or beam-like structures with lower height-to-length ratios and can reduce overall bending stiffness [32–34].

Moreover, to get a deeper analysis of the blade's Tip Displacement over time, the Load-Tip Displacement curve of the *Nlgeom w/ DE* analysis is closely examined towards the end of the loading step. One can observe the non-linear behaviour of the Tip Displacement starting to form at $U = 7.25m$ and noticeable oscillations appearing just after $U = 7.291m$. This structural response will be further analysed in the following sections, alongside relevant damage parameters that will clarify the origin of the non-linear behaviour.

Moment-Tip Rotation Curve for *BLC2* Loading Case. Starting with *BLC2* (simplest to analyse), the curve is represented by a moment-tip rotation plot because the loading condition is a moment applied at the tip of the blade. This provides a more accurate and direct representation of the system's behaviour, since the response of the structure is primarily governed by rotational effects. The moment and the rotation of the tip are calculated by Abaqus over time and their values are extracted from the half-chord point at Section 100 (the tip) as a concentrated moment (*CM3*) and as a rotational displacement (*UR3*) respectively. These variables are predefined in the *Step* module in the *Field Output* and in the *History Output*, before running the simulation. The moment-tip rotation plot is represented in Figure 13.

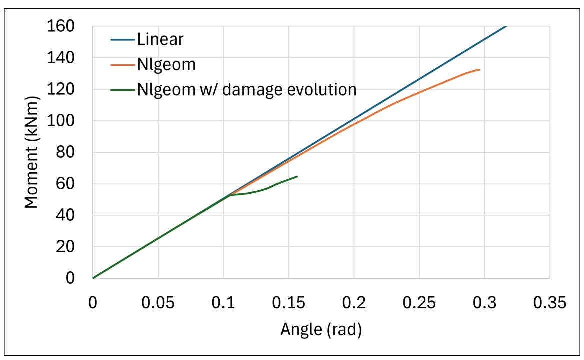

FIGURE 13: MOMENT-TIP ROTATION CURVE FOR *BLC2* LOADING CONDITION

Note that the linear analysis plot is not fully displayed in the figure, as it continues as a straight line (until $CM3 = 450kNm$) and therefore has little additional value to this analysis. Hence, the figure has been adjusted to emphasise the non-linear behavior of the other curves, which is more relevant to fulfill the objectives of this study. The other two simulations are aborted by Abaqus before they converged because the required time increment for convergence is smaller than the minimum time increment specified in the analysis settings. However, lowering this parameter would increase the computational power required to run the simulation of an already intricate system with minimal added benefit to the analysis.

In contrast to linear analysis, where load and deformation are directly proportional, the *Nlgeom* analysis shows that after a certain point, the load required to achieve further deformation increases less rapidly, indicating the effect of strain softening. This happens because the structure is undergoing large deformations, which can lead to a change in the load path or distribution of forces within the structure, and potentially resulting in a reduction of apparent stiffness. Thus, this softening is not due to material degradation or damage but rather geometric non-linearities. In specific, it arises from considering the actual deformed shape of the blade at each step of the analysis, which affects the internal forces and moments within the structure.

The *Nlgeom w/ DE* analysis shows a different structural behaviour when compared to *Nlgeom* curve, roughly starting at *UR3* = 0.11 rad. In addition to the non-linearities captured by the *Nlgeom* analysis, the *Nlgeom w/ DE* analysis takes into account the stiffness degradation as damage evolves, leading to a reduction in the ability for the structure to carry load, which is reflected in the increased degree of softening of the green curve. Also, it can be observed that the *Nlgeom w/ DE* curve reaches the limit of proportionality faster than the *Nlgeom* curve, whereas the linear curve continues straight. Hence, increasing the complexity of the simulation will capture the start of non-linear behaviour of the overall structure at an earlier stage. This indicates a more accurate and reliable representation of the DTU 10MW-RWT.

To analyse the differences in non-linear behaviour, a 2D plot of the tip cross-section is studied at two different time instances, that correspond to different values of moment applied (*CM3*). In order to enhance the contrast in non-linear behavior with the linear plot, the time instances chosen correspond to the points where each of the non-linear simulations are aborted by Abaqus (Figure 14):

- *Nlgeom* at $CM3 = 132.38kN$
- *Nlgeom w/ DE* at $CM3 = 64.51kN$

The *Nlgeom* cross-section shows a considerable deflection from its undeformed shape (more than 150% than that of the linear cross-section). The *Nlgeom w/ DE* is only compared to the linear analysis because the linear and the *Nlgeom* plots are practically equivalent at the time instance analysed. It shows a smaller deviation from the linear deformed cross-section, but this deviation becomes significant when considered over the loading timeline. This implies that if the analysis is extended the deflection would be expected to be much larger than predicted by the *Nlgeom* deflection.

6.2.2 Progressive Failure Analysis (PFA).

PFA for *BLC1* Loading Case. The stresses in this analysis are quite well distributed except for a single point, which shows a stress concentration (Figure 15). This coincides with one of the loading points of concentrated forces from *BLC1* loading case (the one located at $z = 84.8m$ in Table 3). By zooming in the location of maximum stress, one can observe a discontinuity in the stress distribution between elements of the mesh (Figure 15b).

The next part represents a PFA of the four damage mechanisms predicted by Hashin's damage criterion. Similarly to what is done for *BLC2* loading case, the locations where damage is maximum are analysed and their corresponding damage variable is plotted with respect to the time of the loading step ($0.3242s$). This is represented in Figure 16. Damage is present in all four failure

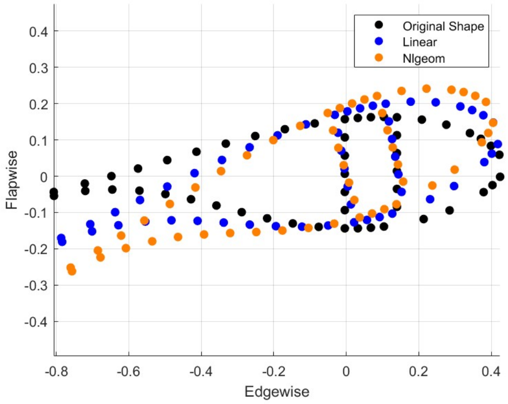

(a) ***Linear*** **and** ***Nlgeom*** **at** $CM3 = 132.38kNm$

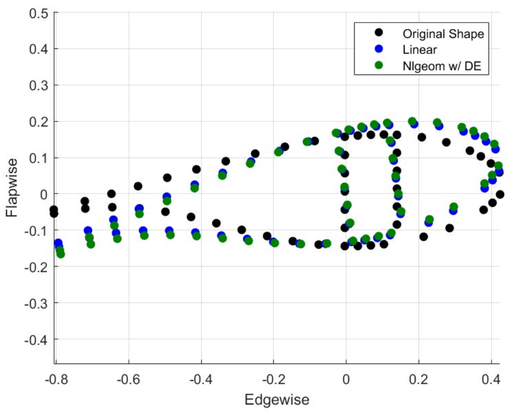

(b) ***Linear*** **and** ***Nlgeom w/ DE*** **at** $CM3 = 64.51kNm$

FIGURE 14: 2D PLOT OF THE TIP CROSS-SECTION IN UNDEFORMED SHAPE AND ROTATING TO DEFORMED SHAPES WITH *BLC2* LOADING

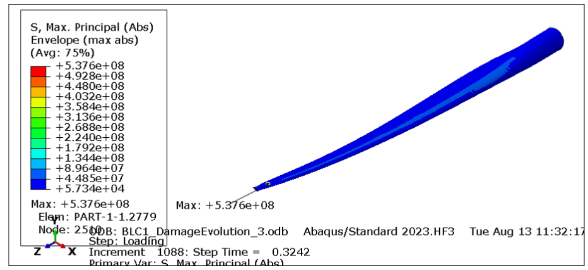

(a) Original plot

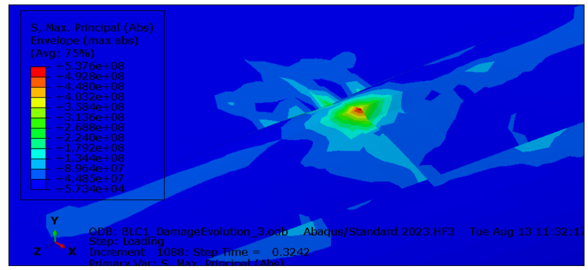

(b) Zoomed in plot at maximum stress

FIGURE 15: MAXIMUM PRINCIPAL STRESSES (ABS) FOR *BLC1* LOADING CASE

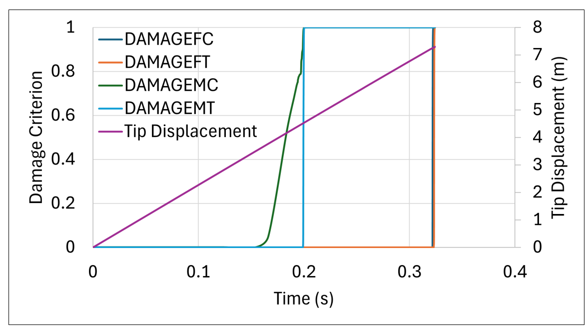

FIGURE 16: DAMAGE VARIABLES (FOR INITIATION AND EVOLUTION) AND TIP ROTATION OVER TIME FOR *BLC1* LOADING CASE

modes so the following damage parameters are used to analyse failure: DAMAGEFT and DAMAGEFC for fiber tension and compression respectively, and DAMAGEMT and DAMAGEMC for matrix tension and compression respectively. In the same plot, Tip Displacement is included to analyse the overall structural behaviour of the blade, while comparing it to the local damage variables.

DAMAGEMC: Damage in matrix compression develops in the lower Cap layup around the same axial position as the stress concentration point that is identified. DAMAGEMC initiates at $t = 0.1662s$ and rises gradually until it reaches 1 at $t = 0.2020s$. So, it takes 0.0358 for damage to develop to complete failure at the point of maximum DAMAGEMC. The final distribution is shown in Figure 17. It can be clearly observed that damage accumulates in the Cap and the Leading and Trailing Panels that are adhesively connected, and develops at their interface. This can be observed in Figure 18, by removing either the Cap (Figure 18a) or the Leading and Trailing Panels (Figure 18b).

DAMAGEMT: Very similar to damage in matrix compression but with a sudden increase of DAMAGEMT from zero to one at $t = 0.1840s$. Damage initiates at the same location as DAMAGEMC, and propagates around that region at the interface between the box-grinder structure with the Leading and Trailing Panels (Figure 19).

DAMAGEFC: Over the loading history, damage in fiber compression develops at a single point located in Web A. This damage variable remains at zero until $t = 0.3218s$. Then, damage initiates at $t = 0.3219s$ (Figure 20a), and rapidly spikes above 1 at $t = 0.3220s$ (Figure 20b). This means that, in that point, it takes less than $0.0002s$ for damage to initiate and develop to complete stiffness degradation.

DAMAGEFT: Damage in fiber tension behaves very similarly to fiber compression. Damage is concentrated at the same point (as fiber compression), which is shown Figure 21. Damage initiates a bit later than DAMAGEFC (at $t = 0.3232$) and rapidly rises above 1 at $t = 0.3235s$, indicating a gap of less than $0.0003s$ for DAMAGEFT to increase from zero to complete damage.

Tip Displacement: Increases linearly with time throughout the

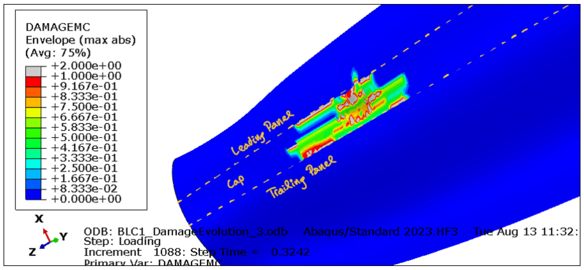

FIGURE 17: DAMAGEMC PLOT AT t = 0.3242s (ZOOMED IN AT MAXIMUM DAMAGE LOCATION)

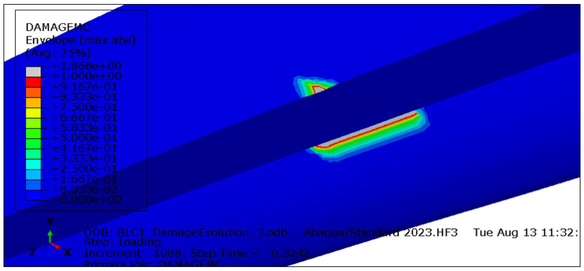

(a) CA layup removed

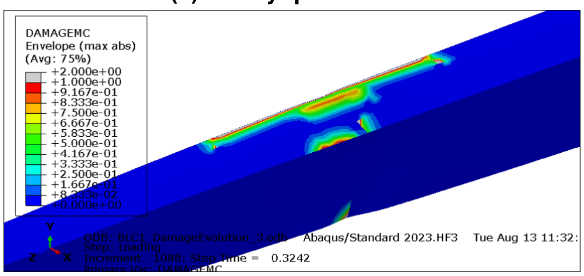

(b) LP and TP layups removed

FIGURE 18: DAMAGEMC ZOOMED IN AT MAXIMUM DAMAGE LOCATION AT t = 0.3242s

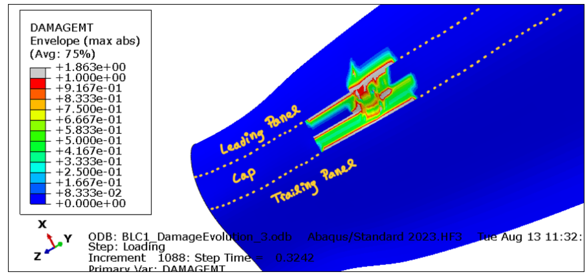

FIGURE 19: DAMAGEMT PLOT AT t = 0.3242s (ZOOMED IN AT MAXIMUM DAMAGE LOCATION)

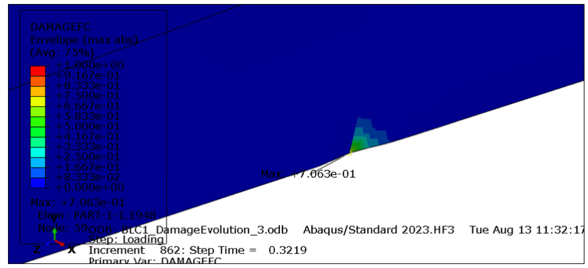

(a) t = 0.3219s

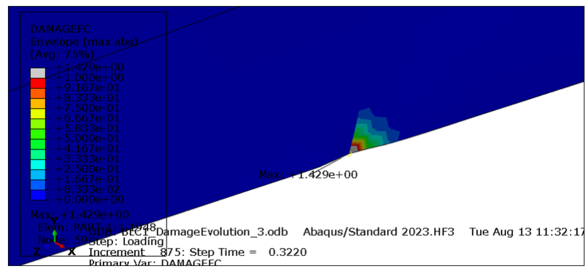

(b) t = 0.3220s

FIGURE 20: DAMAGEFC ZOOMED IN AT MAXIMUM DAMAGE LOCATION

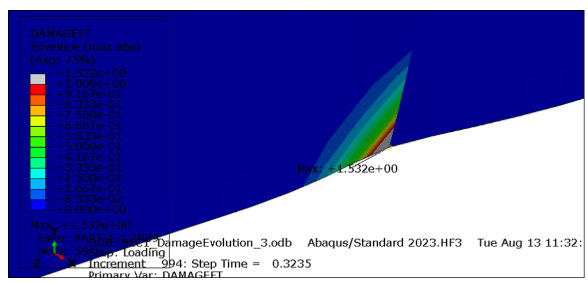

FIGURE 21: DAMAGEFT ZOOMED IN AT MAXIMUM DAMAGE LOCATION AT t = 0.3235s

whole loading step, which indicates a consistent displacement even as damage criteria are met. However, as demonstrated in Section 6.2.1, towards the end of the loading step the Tip Displacement begins to experience some non-linear behaviour. By zooming in on Figure 16, it can be observed that this behavior coincides with the increase in damage evolving in fiber compression failure mode.

PFA for *BLC2* Loading Case. The stress distribution of the deformed shape of this analysis peaks at the tip, which coincides with the place where the loading condition is applied, and dissipates along the blade towards the root (Figure 22). In addition, the stresses are greater at the Leading and Trailing Panels compared to the layups forming the box-grinder structure (Webs and Caps), and stress concentrations appear at the tip, at the interface between the Leading or Trailing panels with the box-grinder. This behaviour is naturally expected because interface areas are typically more prone to failure, mainly due to geometrical and material discontinuities and load transfer properties.

For each of the four damage mechanisms previously described (Section 3.1), the locations where damage is maximum are analysed. Figure 23 is a plot of the damage variables in each of the four failure modes evolving with respect to the time of the loading step (0.1433s). For fiber tension and compression, DAMAGEFT=0 and DAMAGEFC=0 for the entire blade, so damage did not initiate in the fibers. Hence, the variables HSNFTCRT and HSNFCCRT are used instead to measure how close damage is from initiating in the fibers. However, damage did initiate for matrix tension and compression and so variables DAMAGEMT and DAMAGEMC are used to quantify damage evolution in the

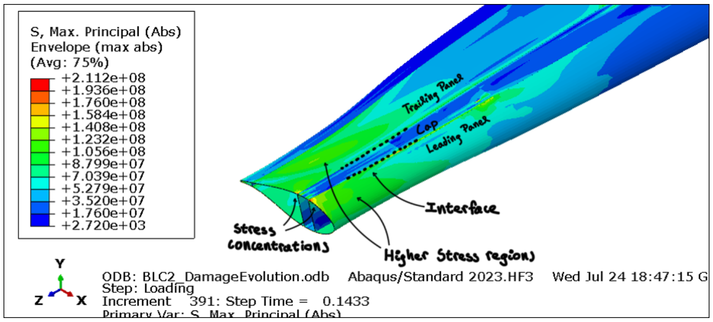

FIGURE 22: MAXIMUM PRINCIPAL STRESSES (ABS) FOR *BLC2* LOADING CASE

structure. Tip rotation is also plotted in the same figure to compare the damage variables (that measure damage locally) to the overall structural behavior of the blade.

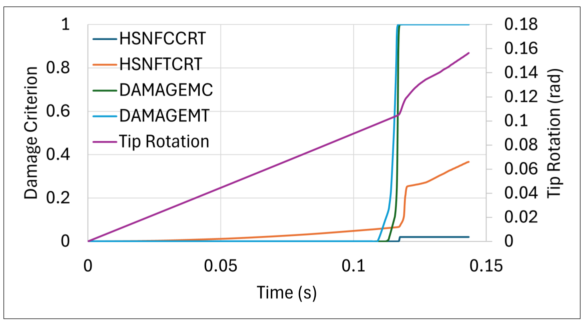

FIGURE 23: DAMAGE VARIABLES (FOR INITIATION AND EVOLUTION) AND TIP ROTATION OVER TIME FOR *BLC2* LOADING CASE

DAMAGEMC: This curve starts to increase at $t = 0.1131s$ and quickly rises to 1 (at $t = 0.1166s$), indicating a rapid propagation of damage until ultimate failure in matrix compression mode. Damage in the matrix compression mode starts very localised. By zooming in and by removing the Nose and Leading Panels layups, one can observe that this area is located at the upper Cap, at the interface between the upper Leading Panel and the box-grinder structure (Figure 24). The damage then propagates in the upper Cap, along this interface and the one between the Cap and the Trailing Panel (Figure 25).

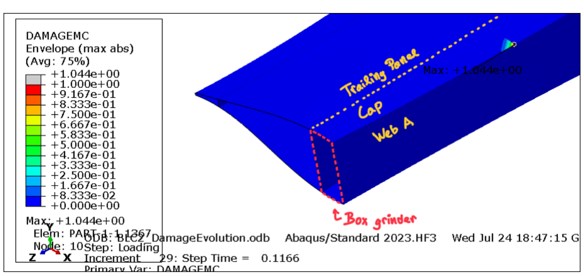

FIGURE 24: DAMAGEMC PLOT AT $t = 0.1166s$

DAMAGEMT: Similar to DAMAGEMC, but with a more gradual increase, starting at $t = 0.1120s$ and peaking slightly before DAMAGEMC, at $t = 0.1154s$. This indicates a slightly anticipated and also intense damage evolution in matrix tension. With regards to damage propagating along the structure, It is shown that damage begins very localised in the upper Cap along the interface with the upper Trailing Panel. This can be better visualized by removing the Trailing Panels and all the layups after (Web C, Tail A, Tail B, Tail C and Tail V), as shown in Figure 26. The damage then develops along the interfaces of the Cap with the Leading and Trailing Panels (Figure 27).

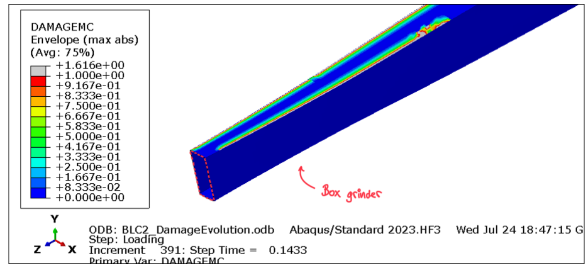

FIGURE 25: DAMAGEMC PLOT AT $t = 0.1433s$ (ZOOMED IN PLOT OF BOX-GRINDER STRUCTURE)

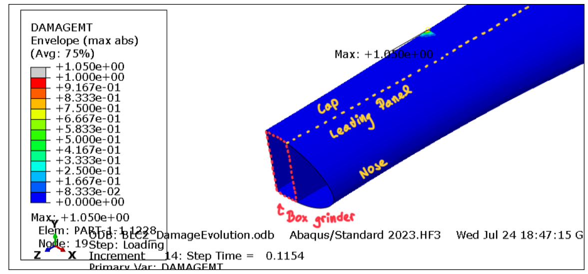

FIGURE 26: DAMAGEMT PLOT AT $t = 0.1154s$ (ZOOMED IN PLOT OF BOX-GRINDER STRUCTURE)

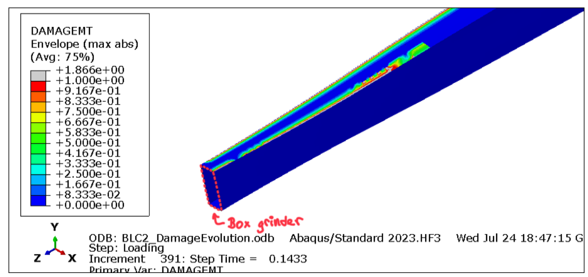

FIGURE 27: DAMAGEMT PLOT AT $t = 0.1433s$ (ZOOMED IN PLOT OF BOX-GRINDER STRUCTURE)

HSNFCCRT: It is practically zero and increases slightly at about $t = 0.12s$. This indicates that the fibers in the structure are still well below the threshold for initiating damage under compression.

HSNFTCRT: It increases linearly until almost $t = 0.12s$. After this point, there is a spike in HSNFTCRT. Hence, the evolution of this variable is studied at the time instance just before and just after this sudden increase, from $t = 0.1090s$ to $t = 0.1192s$ which is shown in Figure 28. In each of them, the red square on the tip rotation plot on the left represents a zoomed-in view that corresponds to the HSNFTCRT plot on the right. The evolution of the HSNFTCRT parameter is clear from one time instance to the other, and develops at the top of Web A, where it adhesively connects to the top Cap, and is more concentrated at the tip. This sudden increase in HSNFTCRT happens just after DAMAGEMT and DAMAGEMC reach 1, and so is likely to come as a consequence of the blade damage that has accumulated in the matrix.

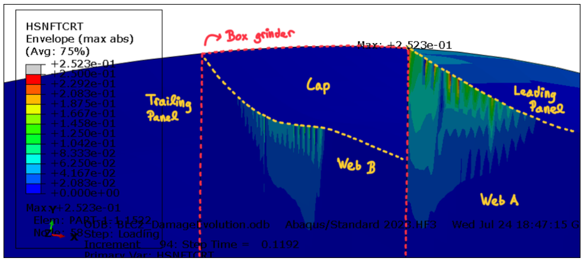

FIGURE 28: DEFORMED SHAPE OF THE DTU-10MW-RWT WITH *BLC2* LOADING AT T=0.1192S (HSNFTCRT)

Tip Rotation: The rotation of the blade's tip follows a linear increase over time until around $t = 0.12s$. Beyond this point, the slope increases significantly, coinciding with the rapid increase in damage criteria of the matrix, suggesting that as the blade tip rotates, it induces a sharp increase in the damage to the blade.

7. CONCLUSION

This research developed progressively complex models for WTBs, using high-fidelity finite element analysis to evaluate structural performance. The DTU 10MW-RWT blade served as a basis for comparing different modelling approaches, validating material properties, and demonstrating accuracy against literature benchmarks. The study focused primarily on shell models, assessing their balance of computational efficiency and detail in characterising WTBs.

Key findings indicate the critical role of incorporating non-linear geometric effects and progressive damage modelling to accurately predict structural responses under realistic loading conditions. Analysis under *BLC1* and *BLC2* loading cases revealed that increased model complexity—progressing from linear elastic to non-linear geometric analysis with damage evolution—significantly improved the accuracy of predicting damage initiation and evolution, highlighting regions prone to failure, particularly under high-stress concentrations.

Ultimately, this work provides a pathway for optimising WTB structural models, aiming for a balance between computational efficiency and accuracy to support the sustainable development of wind energy technologies.

REFERENCES

[1] Kumar, Yogesh, Ringenberg, Jordan, Depuru, Soma Shekara, Devabhaktuni, Vijay K., Lee, Jin Woo, Nikolaidis, Efstratios, Andersen, Brett and Afjeh, Abdollah. "Wind energy: Trends and enabling technologies." *Renewable amp; sustainable energy reviews* Vol. 53 (2016): pp. 209–224. DOI 10.1016/j.rser.2015.07.200. URL https://www.sciencedirect.com/science/article/pii/S1364032115009016. páginas 2

[2] Comission, European. "Communication from the Commission to the European Parliament, the Council, the European Economic and Social Committee and the Committee of the Regions: A New Pact on Migration and Asylum." Technical report no. 2020. URL arXiv:1011.1669v3. páginas 2

[3] Liu, Pu and Barlow, Claire Y. "Wind turbine blade waste in 2050." *Waste management (Elmsford)* Vol. 62 (2017): pp. 229–240. URL https://www.sciencedirect.com/science/article/pii/S0956053X17300491. páginas 2

[4] Chen, Xiao and Eder, Martin A. "A Critical Review of Damage and Failure of Composite Wind Turbine Blade Structures." *IOP Conference Series: Materials Science and Engineering* Vol. 942 No. 1 (2020): p. 012001. DOI 10.1088/1757-899X/942/1/012001. URL https://dx.doi.org/10.1088/1757-899X/942/1/012001. páginas 2

[5] Taglialegne, Luca. "Analytical study of stress fields in wind turbine blades." Ph.D. Thesis, Università degli Studi di Firenze. 2018. URL https://hdl.handle.net/2158/1152810. páginas 2

[6] Tüfekci, Mertol, Ömer Ekim Genel, Tatar, Ali and Tüfekci, Ekrem. "Dynamic Analysis of Composite Wind Turbine Blades as Beams: An Analytical and Numerical Study." *Vibration* Vol. 4 No. 1 (2021): pp. 1–15. DOI 10.3390/vibration4010001. páginas 2

[7] Daniel, I. M. "Failure of Composite Materials." *Strain* Vol. 43 No. 1 (2007): pp. 4–12. DOI 10.1111/j.1475-1305.2007.00302.x. páginas 2

[8] Fremmelev, Mads Anker, Ladpli, Purim, Orlowitz, Esben, Dervilis, Nikolaos, McGugan, Malcolm and Branner, Kim. "A full-scale wind turbine blade monitoring campaign: detection of damage initiation and progression using medium-frequency active vibrations." *Structural health monitoring* Vol. 22 No. 6 (2023): pp. 4171–4193. DOI 10.1177/14759217231163471. páginas 2

[9] Haselbach, Philipp Ulrich and Branner, Kim. "Initiation of trailing edge failure in full-scale wind turbine blade test." *Engineering fracture mechanics* Vol. 162 (2016): pp. 136–154. DOI 10.1016/j.engfracmech.2016.04.041. páginas 2

[10] Bhangale, J.A. "Fatigue analysis of wind turbine blade materials using a continuum damage mechanics framework." Ph.D. Thesis. 2021. DOI 10.4233/uuid:7ea21785-c7ec-49db-85c4-d2e2f6ce6e9b. páginas 2

[11] Montesano, John, Chu, Hao and Singh, Chandra Veer. "Development of a physics-based multi-scale progressive damage model for assessing the durability of wind turbine blades." *Composite structures* Vol. 141 (2016): pp. 50–62. DOI 10.1016/j.compstruct.2016.01.011. páginas 2

[12] Kong, Changduk, Kim, Taekhyun, Han, Dongju and Sugiyama, Yoshihiko. "Investigation of fatigue life for a medium scale composite wind turbine blade." *International journal of fatigue* Vol. 28 No. 10 (2006): pp. 1382–1388. DOI 10.1016/j.ijfatigue.2006.02.034. páginas

[13] Shigley, J. E. and Mischke, C. R. *Mechanical Engineering*, eighth edition ed. BudynasNisbett (2008). páginas 2

[14] Greaves, Peter Robert. "Fatigue Analysis and Testing of Wind Turbine Blades." Ph.D. Thesis, Durham University. 2013. URL https://etheses.dur.ac.uk/7303/1/Fatigue_analysis_and_testing_of_wind_turbine_blades-Hand_in_version.pdf. Doctoral thesis. páginas 2

[15] Laird, Daniel, Montoya, Felicia and Malcolm, David. *Finite Element Modeling of Wind Turbine Blades*. 43rd AIAA Aerospace Sciences Meeting and Exhibit, 43rd AIAA Aerospace Sciences Meeting and Exhibit. American Institute of Aeronautics and Astronautics (2005): DOI 10.2514/6.2005-195. páginas 2

[16] Castro, Oscar and Branner, Kim. "Effect of tunneling cracks on structural property degradation of wind turbine blades." *Composite structures* Vol. 268 (2021): p. 113914. DOI 10.1016/j.compstruct.2021.113914. páginas 2

[17] Júnior, Celso Jaco Faccio, Cardozo, Ana Carolina Pegoraro, Júnior, Valdemar Monteiro and Neto, Alfredo Gay. "Modeling wind turbine blades by geometrically-exact beam and shell elements: A comparative approach." (2018). DOI 10.1016/j.engstruct.2018.09.032. páginas 2

[18] Tavares, Rodrigo P., Bouwman, Vincent and Paepegem, W. Van. "Finite element analysis of wind turbine blades subjected to torsional loads: Shell vs solid elements." *Composite structures* Vol. 280 (2022): p. 114905. DOI 10.1016/j.compstruct.2021.114905. páginas 2

[19] Blasques, J. P., Bitsche, R. D., Fedorov, V. and Lazarov, B. S. "Accuracy of an efficient framework for structural analysis of wind turbine blades." (2015). URL https://onlinelibrary.wiley.com/doi/10.1002/we.1939. páginas 2, 5, 6

[20] Bertolini, Paola, Sarhadi, Ali, Stolpe, Martin and Eder, Martin A. "Comparison of Stress Distributions between Numerical Cross-Section Analysis and 3D Analysis of Tapered Beams." *Proceedings of the 2019 International Conference on Composite Materials*. 2019. RMIT University. URL https://orbit.dtu.dk/files/239536915/2019_TWST_Bertolini_et_al_Taperedbeams.pdf. páginas 2

[21] Bitsche, Robert. "Modelling of Wind Turbine Blades with ABAQUS." (2015). URL https://orbit.dtu.dk/en/publications/modelling-of-wind-turbine-blades-with-abaqus. páginas 2

[22] Fernandez, Garbiñe, Usabiaga, Hodei and Vandepitte, Dirk. "An efficient procedure for the calculation of the stress distribution in a wind turbine blade under aerodynamic loads." (2017). DOI 10.1016/j.jweia.2017.11.003. páginas 2

[23] Tüfekci, Mertol, Öztekin, Vehbi, Pir, İnci, Alioğlu, Murat, Dikicioğlu, Can, Dikicioğlu, Adnan and Tüfekci, Ekrem. "Low strain rate mechanical performance of balsa wood and carbon fibre-epoxy-balsa sandwich structures." *Composites Part C: Open Access* Vol. 12 No. November (2023): p. 100416. DOI 10.1016/j.jcomc.2023.100416. URL https://linkinghub.elsevier.com/retrieve/pii/S2666682023000725. páginas 2

[24] Ullah, Himayat, Alam, Khurshid, Iqbal, Muhammad, Husain, Afzal and Silberschmidt, Vadim V. "Simulation of buckling-driven progressive damage in composite wind turbine blade under extreme wind loads." *Engineering failure analysis* Vol. 140 (2022): p. 106574. DOI 10.1016/j.engfailanal.2022.106574. páginas 2

[25] Bak, Christian et al. "The DTU 10-MW Reference Wind Turbine." Technical report no. DTU Wind Energy. 2013. URL https://backend.orbit.dtu.dk/ws/portalfiles/portal/55645274/The_DTU_10MW_Reference_Turbine_Christian_Bak.pdf. páginas 3

[26] Verma, Amrit Shankar, Vedvik, Nils Petter and Gao, Zhen. "Numerical assessment of wind turbine blade damage due to contact/impact with tower during installation." *IOP Conference Series: Materials Science and Engineering* Vol. 276 No. 1 (2017): p. 012025. DOI 10.1088/1757-899X/276/1/012025. URL https://dx.doi.org/10.1088/1757-899X/276/1/012025. páginas 3

[27] Hashin Z, Rotem A. "A Fatigue Failure Criterion for Fiber Reinforced Materials." *Journal of Composite Materials* Vol. 7(4) (1973): pp. 448–464. DOI doi:10.1177/002199837300700404. URL https://journals.sagepub.com/doi/10.1177/002199837300700404. páginas 4

[28] Hashin, Z. "Failure Criteria for Unidirectional Fiber Composites." *Journal of Applied Mechanics* Vol. 47 No. 2 (1980): pp. 329–334. DOI 10.1115/1.3153664. URL https://asmedigitalcollection.asme.org/appliedmechanics/article-pdf/47/2/329/5878334/329_1.pdf, URL https://doi.org/10.1115/1.3153664. páginas 4

[29] Dassault Systèmes. "Abaqus Analysis User's Manual, Version 6.6." Online (2009). URL https://classes.engineering.wustl.edu/2009/spring/mase5513/abaqus/docs/v6.6/books/usb/default.htm?startat=pt05ch19s03abm41.html. Accessed: 01/08/2024. páginas 4, 5

[30] Camanho, Pedro P., Davila, Carlos G. and de Moura, Mário F. "Numerical Simulation of Mixed-Mode Progressive Delamination in Composite Materials." *Journal of Composite Materials* Vol. 37 No. 16 (2003): pp. 1415–1438. DOI 10.1177/0021998303034505. URL https://journals.sagepub.com/doi/abs/10.1177/0021998303034505?casa_token=kaIioCX_uvMAAAAA:o7POF_iMth7PjLV2dsfCIiswS0q8DdbIDmLFE0ZwrjBTDPB7ScHVWAe1
páginas 5

[31] Camanho, Pedro P. and Davila, Carlos G. "Mixed-Mode Decohesion Finite Elements for the Simulation of Delamination in Composite Materials." Technical Memorandum NASA/TM-2002-211737. NASA Langley Research Center. 2002. URL https://ntrs.nasa.gov/citations/20020053651. páginas 5

[32] da Silva, M. R. M. Crespo and Glynn, C. C. "Nonlinear flexural-flexural-torsional dynamics of inextensional beams." *International Journal of Solids and Structures* Vol. 14 No. 1 (1978): pp. 93–107. URL https://doi.org/10.1016/0020-7683(78)90021-6. páginas 8

[33] Antman, Stuart S. *Nonlinear Problems of Elasticity*, 2nd ed. Springer (2005). páginas

[34] Librescu, Liviu and Song, Oh. *Thin-Walled Composite Beams: Theory and Application*. Springer (2006). páginas 8

